ELSEVIER

Contents lists available at ScienceDirect

CIRP Annals - Manufacturing Technology

journal homepage: https://www.editorialmanager.com/CIRP/default.aspx



In-situ blended 316L-Si and PH48S via laser directed energy deposition for functionally graded applications



Rujing Zha^a, Nhung Thi-Cam Nguyen^b, Gregory B. Olson^c, Jian Cao (1)^{a,b,*}

a Department of Mechanical Engineering, Northwestern University, Evanston, IL, USA b Department of Materials Science and Engineering, Northwestern University, Evanston, IL, USA

Department of Materials Science and Engineering, Massachusetts Institute of Technology, Cambridge, MA, USA

ARTICLE

INFO

Article history: Available online 23 May 2024

Keywords: Additive manufacturing Stainless steel Functional graded material

ABSTRACT

Laser powder blown directed-energy deposition (DED) enables the flexible fabrication of functionally gradient structures. In the region where multiple feedstocks are blended, it is natural to apply the 'rule of mixtures'. Here, we show that by blending PH48S and 316L-Si steel powders using DED, the resulting material

possesses lower yield strength but increased hardening and a secondary hardening regime not observed in the original alloys, invalidating direct interpolation between feedstock properties. Microstructural analysis of the mixed material revealed a solidification-driven multi-phase hierarchal microstructure. This result enables greater accuracy and increased design space in the co-design of materials and manufacturing processes.

© 2024 CIRP. Published by Elsevier Ltd. All rights are reserved, including those for text and data mining, Al training, and similar technologies.

1. Introduction

Parts designed using functionally graded materials (FGM) place specific materials precisely where they are needed to locally optimize competing material properties, such as stiffness and density, thus exceeding the performance of single-material parts or offering comparable performance at reduced cost and weight. While several technologies in both the powder-bed and directed-energy deposition additive manufacturing (AM) families may be used to fabricate FGMs [1], laser-powder directed energy deposition (DED) stands out due to its ability to mix multiple feedstocks on-the-fly and its high design freedom in building and gradient direction.

To fully take advantage of the freedom afforded by FGMs, topology optimization works have been expanded to have more than just two fundamental components (i.e. solid and void) [2]. However, these works typically have limited themselves to consider only linear constitutive models, such as in Liu et al. [3], partially due to a lack of models for the post-yield behaviour of many materials in the blended region. Nevertheless, an effective part design using either as-built FGMs or hybrid manufacturing processes (e.g., AM followed by forging or shot peening) requires accurate characterization of the hardening behaviour of mixed materials.

Much of the work on metal FGMs fabricated using DED centers on combining materials from different alloy systems, such as Ti alloys, steel, and Ni superalloys, as well as combinations between metallic and ceramic materials [1]. Due to the formation of undesirable intermetallic phases in the mixed region, defects often arise, such as cracking and delamination. These multi-alloy system works have

E-mail address: jcao@northwestern.edu (J. Cao).

https://doi.org/10.1016/j.cirp.2024.04.041

therefore focused on defect mitigation (e.g. in [4]) and have not generally reached the stage of generating useful material parameters in the mixed region for design.

In recent years, there has been renewed interest in the development of high-performance stainless steels as a low-cost substitute for more exotic materials. Due to the sheer variety of mechanical behaviours available, from high yield strength precipitation hardened alloys such as 17-4PH to more formable alloys such as 316L and 304, there is considerable variety in base mechanical behaviours for use in a functionally graded, optimized structure. Simultaneously, the substantial overlap in primary alloying constituents reduces the risk of forming deleterious phases, which cause the brittle cracking common in mixed alloy systems. Yet, due to the wide range of strengthening mechanisms in stainless steel, the mechanical response cannot be directly interpolated between two extremes, especially when alloys of different primary strengthening mechanisms are combined.

Previous works have addressed some aspects of functional gradation while using stainless steel as a base material. For example, Dash and Bandyopadhyay [5] explored the properties of DED specimens fabricated using a 50/50 premixed blend of 316L and 17-4PH stainless steels. They found that the specimen exhibited a reduced yield strength compared to the base components; however, they did not test to high strains and only considered specimens in compressive loading.

This work aims to explore the properties of mixed steel from two families of engineering steels. 316L-Si is selected as a representative work-hardening strengthened, highly ductile steel, whereas PH48S is selected as a direct contrast due to its high yield strength but lower total elongation before failure. These results can guide the optimal design of a future hybrid manufactured part.

^{*} Corresponding author.

2. Experimental setup

2.1. Feedstock powders

Feedstocks consisted of commercial 316L-Si austenitic stainless steel and PH48S stainless-steel powder. Oerlikon Metco supplied the 316L-Si powder, with a size distribution of 66150 mm (P/N: 1079454). Carpenter Additive supplied the PH48S powder as Micromelt Ferrium PH48S, for which LPW Technologies sieved to particle sizes of 53150 mm.

2.2. DED setup

Coupons were fabricated using laser DED on the Additive Rapid Prototyping Instrument (ARPI), a custom open-architecture DED machine at Northwestern University. A 1070 nm wavelength fiber laser (IPG YLR-1000) shines on the substrate via a Precitec optics head attached to a three-stage Aerotech gantry, while an annular coaxial nozzle (Fraunhofer COAX8) delivers the powder stream via argon carrier gas (<10 ppm impurities). The powder metering system consists of four rotating-disk powder hopper systems (PowderMotionLabs X2), connected to a single stream via a double-wye junction. This powder stream travels along 1.9 m of tubing to ensure a good powder mixture before being split into four streams that feed the powder nozzle. Additional details about ARPI can be found in Jeong et al. [6].

Deposition parameters used in this study are illustrated in Table 1. These settings correspond to an energy density (ED ½ P=vd) of 38.1 J/mm², and a linear powder density of 3.31 £ 10² g/mm. Process parameters were kept the same for both steels as previous experiments depositing these steels demonstrated similar single clad width and height for both compositions at the same laser and powder flow settings. Three build types were built, each with a scan distance of 45 mm, a layer height of 0.55 mm, and 40 bidirectionally scanned layers. Fig. 1 illustrates the build geometry. In all builds, argon flowed freely from all four hopper systems at the same nominal flow rate to prevent powder backflow. In the first build type, the metering wheels were set to deposit only 316L-Si; in the second type, only PH48S. In the third build type, the 316L-Si and PH48S metering wheels were enabled at 50 % of their original speeds to generate an expected 1:1 ratio of 316L-Si to PH48S. Two walls were fabricated in each type, for a total of six thin walls. All thin walls used low-carbon AISI 1018 disks as the substrate material.

Table 1 Deposition parameters.

Laser Power P	Scan Speed v	¹ Laser e ₂ Diameter	Powder Flow Rate	Carrier Gas Flow	Shield Gas Back Pressure
600 W	7 mm/s	2.24 mm	13.9 g/min	14.2 LPM	172 kPa
0 2 Z X	A Scan Di	5 mm B	~2.5 mm		316L-Si Blend PH48S

Fig. 1. Thin-wall build illustrating locations of tensile specimens (13) and as-built 'pill' coupons (A, B). Results from as-built specimens 13 and pill coupon B are used for the analysis conducted in this work.

2.3. Tensile testing

From each thin wall, 4 tensile bars and 2 'pill' specimens were cut as shown in Fig. 1. The tensile specimens had a reduced parallel section length of 5 mm, and a cross-sectional area of 0.75 mm by

1.2 mm. The 0.75 mm thick flat pills were cut from between adjacent tensile bars. The tensile specimens were painted with a speckle pattern for in-situ digital-image correlation (DIC) during the tensile tests. In this study, tensile

specimens 13 of the first thin wall and 03 of the second wall were used. Metallographic analysis was conducted on pill 'B' of the first thin wall. Tensile bar 0 and pill A from the first wall were reserved for future analysis on the effect of heat treatment. All specimens were tested in the as-built condition.

Tensile tests were conducted using an MTS Criterion C45 universal testing machine with a 2.5 kN load cell under monotonic loading until failure at a crosshead speed of 90 mm/min, corresponding to a nominal strain rate of 3.0 £ $10^4\,\mathrm{s^1}$. Tensile specimens were preserved after failure for fractography of the failure surface. Images were captured using a Point Grey Grasshopper3 color camera (model GS3-U3-28S4C, with a Sony ICX687 CCD sensor) set to monochromatic output equipped with a fixed-focal length lens, with a pixel size of 5.625 mm. DIC images were post-processed using Correlated Solutions VIC-2D software. Strains were recorded from the gauge region of the tensile bar.

2.4. Microstructural characterization

The supplied powders were ground to a cut section to characterize the chemical composition of both powders. The as- built microstructure characterization was conducted in pill 'B' as indicated in Fig. 1. Both powder and as-built specimens were ground and polished to a 0.06 mm finish with a final polishing step of vibratory polishing with colloidal silica over a period of 12 h. The microstructural observation was conducted using a Quanta 650 Scanning Electron Microscope (SEM) equipped with an Energy Dispersive Spectrometer (EDS) and Electron Backscatter Diffraction (EBSD) with Aztec software version 6.1. The EBSD were conducted at 20 kV, with a step size of 0.70.9 mm.

3. Results

3.1. Microstructure of the as-built specimens

Fig. 2 shows the SEM-EDS images of the 316L-Si (a) and PH48S (b) powders, respectively, which are primarily spherical. The EDS chemical quantitative measurement of the cut section of the particle analysis exhibits a homogeneous distribution of all elements in both powders. The experimental chemical quantitation of 316L-Si in wt.% is 17.2-Cr, 12-Ni, 3.0-Mo, 2.0-Si, and 0.5-Mn; while the estimated value for PH48S is 11.4-Cr, 7.9-Co, 9.0-Ni, 1.6-Mo, 0.6-Ti, 0.3-Al.

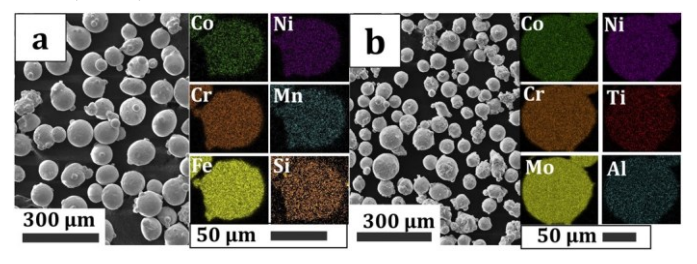


Fig. 2. The morphology and chemical maps through a cross-section of the 316L-Si (a) and PH48S (b) powders. Elements are evenly dispersed with no segregation; sectioned powders are free from porosity.

The Backscattered SEM (BSE) microstructure of all the as-built specimens is presented in Fig. 3. All the specimens show a sound structure with no presence of cracks or delamination. For all three specimen types, the "pill" specimen from location B in the first thin wall was analyzed for porosity by thresholding the image obtained via optical microscopy. The 316L-Si specimen was found to have a porosity of 0.61 %, the PH48S specimen 0.74 %, and the mixed specimen 0.60 %. Observed porosity was primarily the lack-of-fusion type, identifiable by an irregular pore shape. The mixed specimen (c) in Fig. 3 also shows possible gas-type porosity, as indicated by the red dashed circle.

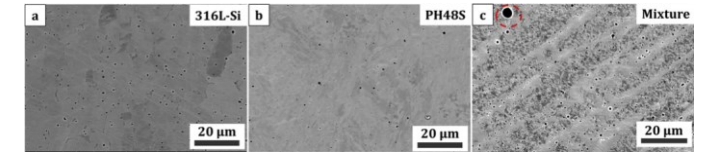


Fig. 3. The BSE microstructure of the as-built (a) 316L-Si, (b) PH48S, and (c) mixture. The red dashed circle in (c) indicates possible gas porosity.

The BSE and the corresponding EDS analysis for the mixed specimen are illustrated by Fig. 4. The contrasting color from the BSE image and the chemical maps of the Si, Fe, and Mo elements clearly show the locations of 316L-Si-like (Si and Mo-rich) and PH48S-like (more Fe-rich) components. The Si and Mo EDS maps indicate that the brighter grey area is close to the 316L-Si stainless steel, while the darker phase islands are PH48S-like. No notable O amount was found in the EDS analysis. The EDS maps of the mixed specimen (Fig. 4) reveal Ti and Al-rich precipitates, whereas the corresponding EDS analysis of the PH48S powder (Fig. 2) shows homogeneous Ti and Al distribution. This indicates possible precipitation incurred by thermal cycling; however, the Ti and Al concentrations are not aligned, and the precipitates do not take the rod-shaped morphology of the h-Ni₃(Ti,Al) precipitates that drive the strength of PH48S [7].

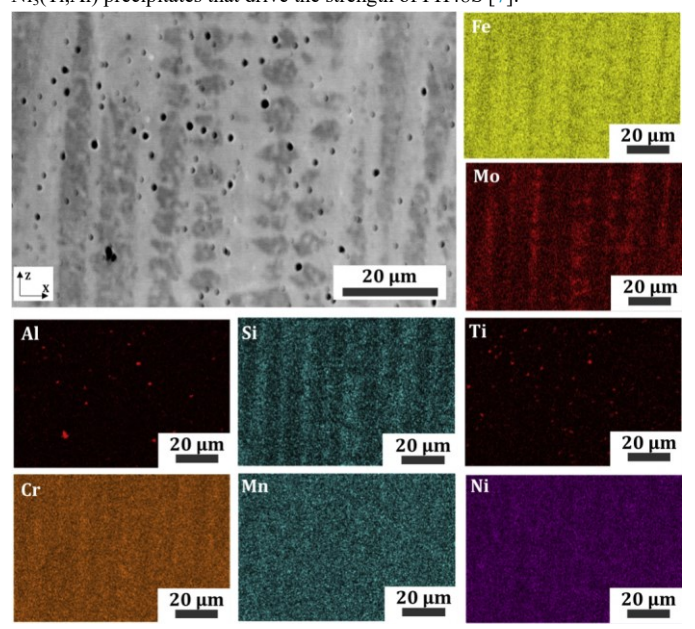


Fig. 4. The BSE-EDS microstructure of the mixed specimen. Light bands are more similar to 316L-Si, as indicated by elevated Si and Mo, whereas elevated Fe in dark regions indicate a composition closer to PH48S. Scattered Al- and Ti- rich precipitates occur throughout.

The EBSD images of the phase map and band contrast from PH48S are presented in Fig. 5. The yellow dashed line indicates the melt pool boundary. The phase map shows that the as-built PH48S is mainly composed of the body-centered cubic (BCC) structure, which is consistent with lath martensite in previous work on PH48S [8]. The as-built PH48S has a fine microstructure with lath-shaped grains, which is more visible in the band contrast image in Fig. 5. Although

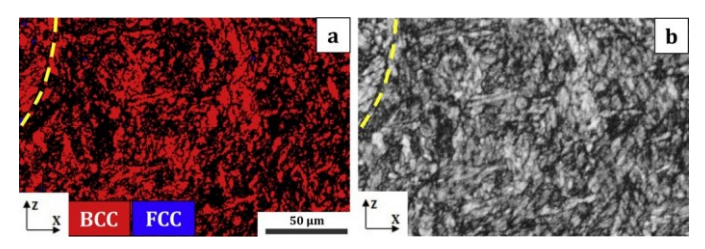


Fig. 5. The EBSD phase map (a), and band contrast (b) of the PH48S as-built specimen. The yellow dashed line indicates the melt pool boundary. Black regions represent unindexed

R. Zha et al. / CIRP Annals - Manufacturing Technology 73 (2024) 137140

locations

140

the EBSD phase map (Fig. 5) shows a BCC phase which may be ferrite (BCC) and/or martensite (body-centered tetragonal (BCT), which appears as BCC in the EBSD map), the characteristic lath shape suggests that the microstructure in the as-built PH48S is martensitic, formed by the high cooling rate in DED.

The equivalent Co and Ni ratio of the mixed specimen is estimated as C_{requ} % %Cr \flat 1:4 %Mo \flat 1:5 %Si \flat 0:5 %Nb \flat %Ti% 20wt% and Ni $_{eq}$ % %Ni \flat 30 % \eth C \flat

NÞþ 0:5 %Mn 11:5wt%; these values fall in the boundary between the Austenite + Martensite + Ferrite zone and the Austenite + Ferrite zone in the Schaeffler diagram [9]. The EBSD phase map of the mixed specimen, shown in Fig. 6, is consistent with this combined microstructure of austenite (FCC), ferrite (BCC), and martensite (BCT). The microstructure of the 316L-Si is composed of primarily austenite with a small amount of ferrite, as widely reported in the literature [10-11]. The BCC assumption from the microstructure of the as-built PH48S and the ratio of an equivalent concentration of Ni and Cr suggest a three-phase microstructure consisting of austenite, ferrite, and martensite in the mixed specimen.

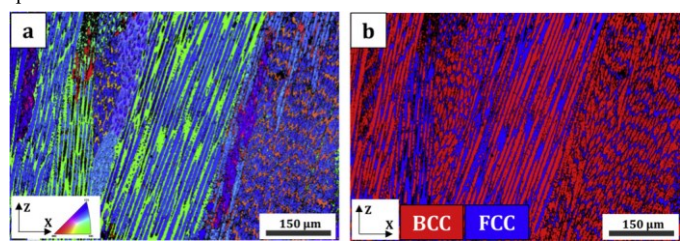


Fig. 6. EBSD of the mixed specimen: (a) IPF color map; and (b) phase map. Black regions represent un-indexed locations.

The microstructure in the mixed specimen demonstrates a unique hierarchal structure, with 'super-grains' consisting of an austenitic matrix embedded with commonly oriented variate aspect 'pseudograins' (Fig. 6, oblong BCC regions) that are further broken down into dark and light regions (Fig. 3, Fig. 4) corresponding to BCC (ferritic/ martensitic) and FCC (austenitic) regions, respectively. We hypothesize that the alternating BCC/FCC grain structure is due to segregation of the alloying elements during solidification rather than incomplete mixing of the base powders, as the pseudo-grains within each 'supergrain' follow a regularly spaced, rectilinear orientation and the super-grain texture consistently extends across melt pool boundaries; furthermore, 'pseudograins' follow the same crystallographic orientation as shown in the inverse pole figure plot.

3.2. Tensile testing results

Fig. 7 illustrates the results of the tensile testing. The PH48S specimens had the highest yield and ultimate strength of these specimens, with relatively little strain before the ultimate tensile strength (UTS) was reached. The average yield and tensile strengths were 471 MPa and 857 MPa, respectively, as expected below the post-heat treatment tensile yield strength of 13501600 MPa for laser DED specimens [7]. This result is quite reasonable, given that PH48S derives much of its

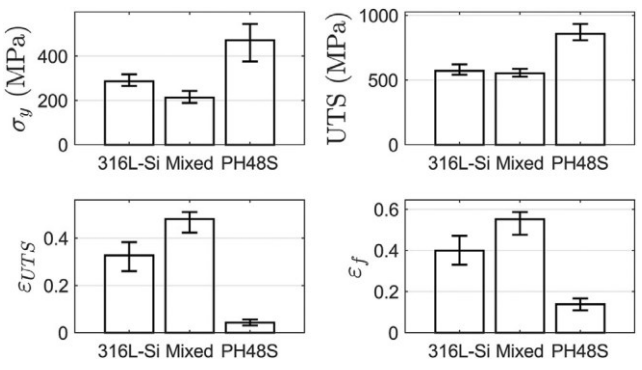


Fig. 7. Summary of yield strength ($s_{\gamma}P$, ultimate tensile strength (UTS), engineering strain at UTS

 $(\varepsilon_{\text{UTS}}\mathsf{P}, \text{ and engineering strain at failure } \mathfrak{d}\varepsilon_{\mathsf{f}}\mathsf{P}.$

strength from hprecipitation formed during aging heat treatment steps, which our specimens did not undergo. The 316L-Si yield strength of 286 MPa and UTS of 572 MPa found in this work are lower-to-similar to that reported in the literature for horizontally oriented DED specimens (411 MPa and 571 MPa, respectively [12]). The maximum extensions of 3647 % are in line with that reported in other previous works. Fractography showed ductile failure in all cases.

Fig. 8 illustrates the true stress-strain response of all specimens until the onset of necking. The mixed steel specimens exhibited three hardening stages: a regime of slow hardening, from yielding up to approximately 2030 % strain, followed by an increase in hardening rate up to the final necking region. This result is similar to that found by Zafri and Xia [13] who used Selective Laser Melting (SLM) to combine highstrength and high-ductility base titanium alloys and found that the resulting hybrid titanium alloy (HYTA) exhibited three-stage hardening, determining that the multiple hardening regimes were due to part inhomogeneity. As different regions harden at different rates, the stress-strain curve follows three distinct stages. The microstructural analysis in Section 3.1 of the present work illustrates a similar effect, with chemically and crystallographically distinct regions with well-connected interfaces enabling smooth transition between the first and second hardening stages. Zafri and Xia's work [13], however, shows segregation indicative of incomplete Marangoni flow-induced mixing due to the reduced melt pool size and higher solidification rates of SLM.

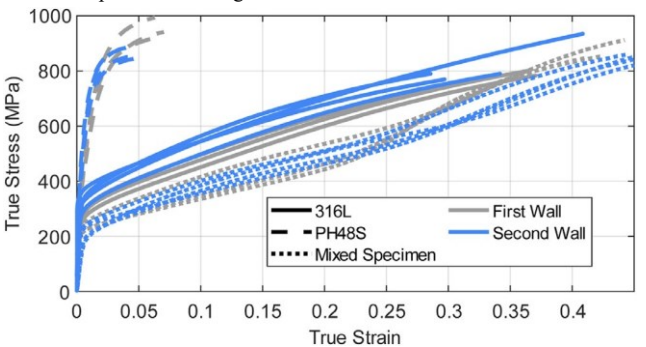


Fig. 8. True stress-strain curve for the 316L-Si, PH48S, and mixed specimens. "First Wall" and "Second Wall" refer to the repetition for each of the three specimen types, for a total of 6 thin walls.

An alternative explanation for the multi-stage hardening seen in the mechanical response is the transformation-induced plasticity effect as observed in the work by Wang et al. [14] on cryogenic deformation of 316L. In that work, the austenitic 316L encountered martensitic transformation after the initial yield point, also resulting in a three-stage hardening curve, with an increase in hardening rate after 1020 % strain. That work, however, explored the hardening at 196 °C rather than at room temperature as seen in the present report. Further works will use X-ray diffraction on the deformed and undeformed regions of the tensile specimens to explore the dominant mechanism behind the three-stage hardening response.

4. Conclusion

In this work, laser-powder DED was used to fabricate specimens of 316L-Si and PH48S stainless steels, as well as a specimen consisting of both powders blended in-situ in a 1:1 ratio. The mixed alloy exhibited reduced yield strength when compared with both base components, but improved ductility and comparable UTS to 316L-Si and a three-stage hardening curve. BSE-EDS of the mixed material revealed a hierarchal microstructure with alternating regions of FCC and BCC structure. The uncommon stress-strain response may arise from the multiscale heterogeneous microstructure, deformation-induced martensitic transformation, or a combination of both. Future work, exploring additional mixing ratios, different strain paths, and loading directions, as well as metallographic analysis of post-deformation specimens, are suggested as these efforts can shed additional light onto the underlying phenomena that drives the unique microstructure as discovered here in this work.

Declaration of competing interest

The authors declare that they have no known competing financial interests or personal relationships that could have appeared to influence the work reported in this paper.

CRediT authorship contribution statement

Rujing Zha: Data curation, Formal analysis, Investigation, Methodology, Validation, Visualization, Writing original draft, Writing review & editing, Conceptualization, Funding acquisition. Nhung Thi-Cam Nguyen: Conceptualization, Data curation, Formal analysis, Investigation,

Methodology, Validation, Visualization, Writing original draft, Writing review & editing. Gregory B. Olson: Conceptualization, Funding acquisition, Resources, Writing review & editing. Jian Cao: Conceptualization, Funding acquisition, Methodology, Project administration, Resources, Supervision, Validation, Writing review & editing.

Acknowledgements

Rujing Zha and Nhung Thi-Cam Nguyen made equal contributions to this work. This work was supported by the National Institute of Standards and Technology (NIST) Center for Hierarchical Material Design (CHiMaD) under grant No. 70NANB19H005, the National Science Foundation (NSF) Graduate Research Fellowship Program (GRFP) under grant No. DGE-2234667, and the NSF Engineering Research Center for Hybrid Autonomous Manufacturing, Moving from Evolution to Revolution (ERC-HAMMER) under Award Number EEC-2133630. QuesTek Innovations, LLC supplied the PH48S feedstock used in this work.

Supplementary materials

Supplementary material associated with this article can be found in the online version at doi:10.1016/j.cirp.2024.04.041.

References

- Ghanavati R, Naffakh-Moosavy H (2021) Additive Manufacturing of Functionally Graded Metallic Materials: A Review of Experimental and Numerical Studies. Journal of Materials Research and Technology 13:1628–1664.
- [2] Sanders ED, Aguilo MA, Paulino GH (2018) Multi-Material Continuum Topolog y Optimization with Arbitrary Volume and Mass Constraints. Computer Methods in Applied Mechanics and Engineering 340:798–823.
- [3] Liu B, Huang X, Cui Y (2022) Topology Optimization of Multi-Material Structures with Explicitly Graded Interfaces. Computer Methods in Applied Mechanics and Engineering 398:115166.
- [4] Bobbio LD, Bocklund B, Otis R, Borgonia JP, Dillon RP, Shapiro AA, McEnerney B, Liu Z-K, Beese AM (2018) Characterization of a Functionally Graded Material of Ti-6Al-4V to 304L Stainless Steel with an Intermediate V Section. Journal of Alloys and Compounds 742:1031–1036.
- [5] Dash A, Bandyopadhyay A (2024) 17-4 PH and SS316L Bimetallic Structures via Additive Manufacturing. Virtual and Physical Prototyping 19:e2292695.
- [6] Jeong J, Webster S, Liao S, Mogonye J-E, Ehmann K, Cao J (2022) Cooling Rate Measurement in Directed Energy Deposition Using Photodiode-Based Planck Thermometry (PDPT). Additive Manufacturing Letters 3:100101.
- [7] Yan F, Chan Y, Saboo A, Shah J, Olson G, Chen W (2018) Data-driven prediction of mechanical properties in support of rapid certification of additively manufactured alloys. Computer Modeling in Engineering & Sciences 117:343–366.
- [8] Pioszak GL, Gangloff RP (2017) Hydrogen Environment Assisted Cracking of a Modern Ultra-High Strength Martensitic Stainless Steel. Corrosion 73:1132–1156.
- [9] Berns H, Gavriljuk V, Shanina B (2008) Intensive Interstitial Strengthening of Stainless Steels. Advanced Engineering Materials 10:1083–1093.
- [10] Belsvik MA, Tucho WM, Hansen V (2020) Microstructural Studies of Direct-LaserDeposited Stainless Steel 316L-Si on 316L Base Material. SN Applied Sciences 2:1967
- [11] Heidowitzsch M, Gerdt L, Samuel C, Maetje J-F, Kaspar J, Riede M, Lopez E, Brueckner F, Leyens C (2023) Grain Size Manipulation by Wire Laser Direct Energy Deposition of 316L with Ultrasonic Assistance. Journal of Laser Applications 35:032017.
- [12] Jackson MA, Morrow JD, Thoma DJ, Pfefferkorn FE (2020) A Comparison of 316 L Stainless Steel Parts Manufactured by Directed Energy Deposition Using GasAtomized and Mechanically-Generated Feedstock. CIRP Annals 69:165–168.
- [13] Zafari A, Xia K (2019) Superior Titanium from Hybridised Microstructures A New Strategy for Future Alloys. Scripta Materialia 173:61–65.
- [14] Wang C, Lin X, Wang L, Zhang S, Huang W (2021) Cryogenic Mechanical Properties of 316L Stainless Steel Fabricated by Selective Laser Melting. Materials Science and Engineering: A 815:141317.